Sixfold, fourfold, and threefold excitations in the rare-earth metal carbide R_2C_3

Lei Jin, Ying Liu,[*] Xiaoming Zhang, Xuefang Dai, and Guodong Liu[†]

State Key Laboratory of Reliability and Intelligence of Electrical Equipment, Hebei University of Technology, Tianjin 300130, China
and School of Materials Science and Engineering, Hebei University of Technology, Tianjin 300130, China

Unconventional fermions, such as threefold, fourfold, sixfold, and eightfold fermions have attracted intense attention in recent years. However, the concrete materials hosting unconventional fermions are still in urgent scarcity. In this work, based on first-principle calculations and symmetry analysis, we reveal rich unconventional fermions in existing compound R_2C_3 (R = Y, La, Ce, Pr, Nd, Sm, Tb, Dy, Ho, Er, Tm, Yb, Lu). We show that these compounds host quadratic dispersive threefold, linear dispersive fourfold, and sixfold points (SPs) near the Fermi level in their electronic band structures when spin-orbital coupling (SOC) is not included. We also find that a uniaxial strain can transform the unconventional fermions into other types of fermions, depending on the directions of strain. When SOC is considered, a SP transforms to an eightfold degenerate point and a fourfold degenerate point. Overall, our work provides a family of realistic materials to study the unconventional fermions.

I. INTRODUCTION

Topological semimetals/metals have been attracting intense research interest in present condensed matter physics [1–5]. Commonly, there are emergence nontrivial band crossings in their electronic band structures near the Fermi level, enforced by topology and symmetry. Hence, the quasiparticles in the low-energy region behave differently from the conventional fermions which are described by the Schrödinger equation. For example, Weyl/Dirac semimetals/metals possess two-/fourfold degenerate band crossings in their band structures, and the quasiparticle around the crossing can be described by the Weyl/Dirac equation which behaves like the Weyl/Dirac fermion in the high energy region [6–26], leading to novel physical phenomena, like the chiral anomaly [16]. Recently, topological semimetals/metals with unconventional fermions, like double Weyl fermion, charge-2 Dirac fermion, spin-1 fermion, sixfold fermion, eightfold fermion, protected by crystalline symmetry are becoming a focusing research field [27–35]. Therefore, it is natural to search the realistic materials to study these unconventional fermions which are accompanied by fascinating physical properties.

Until now, only several materials have been reported that host new types of unconventional fermions. For example, structurally chiral topological semimetals, the CoSi family [36–41], was predicted to host chiral fermions that were characterized by large Chern numbers C (topological charges), namely, spin-1 excitation and double Weyl fermions which have $|C|$=2. Since these fermions locate at the center or corner of the first Brillouin zone, Fermi arcs connecting the nonzero chiral fermions almost span the whole Brillouin zone [40]. Remarkably, due to the absence of mirror symmetries, these two chiral fermions locate at different energies, expected

to display some exotic physical effects, gyrotropic magnetic effect, and quantized circular photogalvanic effect [42,43]. Recently, Takane *et al.* [37] have experimentally demonstrated the existence of these unconventional chiral fermions. Subsequently, a chiral fermion of sixfold degeneracy characterized by $C=\pm 4$ was found in AlPt material verified in experimental and theoretical works [44]. Followingly, $PdSb_2$ [45–47], $PtBi_2$ [48], and $Li_{12}Mg_3Si_4$ [49] are also predicted to possess such a fermion. A few real materials, including compound $TaTe_4$ [50], were predicted to host an eightfold fermion. However, the number of candidates to study the unconventional fermions is limited, and they also have their own disadvantages.

Much effort has been devoted to discovery materials which host unconventional fermions. So far, realistic materials possessing different types of unconventional fermions at the same time are limited. Thus, it is urgent to identify realistic materials with unconventional fermions. According to the symmetry discussion, we have known that the symmetries play an important role in the determination of degeneracy. The space group No. 220 allows multiple degeneracy points to exist. Particularly, the space group No. 220 has been proposed that possesses degenerate points with different degeneracy, namely, threefold, fourfold, and sixfold in the same time. Therefore, materials belonging to No. 220 are good candidates to study the unconventional fermions. In this work, we indeed discover a family of materials with No. 220, R_2C_3, (R = Y, La, Ce, Pr, Nd, Sm, Tb, Dy, Ho, Er, Tm, Yb, Lu), which host six- (SP), four- (FP), threefold degenerate points (TP) at the same time. This family of materials has three advantages. First, the rare-earth sesquicarbides, R_2C_3, (where R is a rare earth) share the same lattice structure (belonging to No. 220). By changing the rare-earth element, there is a trend that the degenerate points are approaching the Fermi level. Hence, we can find a more ideal candidate. Second, besides the degenerate points, there are no other extraneous bands around them; this provides an ideal candidate to study the unconventional

[*]ying_liu@hebut.edu.cn
[†]gdliu1978@126.com

fermions in concrete materials. Third, this family of material has been synthesized in experiments [51–55]. Samples produced by arc melting have critical temperatures Tc of 10–12 K, with little dependence on the particular rare earth. Since the 1960s, research has mainly focused on the investigations of their superconducting, electronic, and thermodynamic properties, electron-phonon coupling, and neutron diffraction [52,56–63]. The intensive studies about this family of materials suggest that they are good candidates to be experimentally detected.

In this work, based on the first-principle calculations and symmetry analysis, we demonstrate that the R_2C_3 family exhibits three types of fermions at high symmetry points, i.e., a sixfold point at H point, a threefold point at Γ point, and a Dirac point at P point. We take Yb_2C_3 as an example to support our discovery. We point out that the reasons for such a choice are at least in two aspects. First, the three unconventional band crossings in Yb_2C_3 are quite close to the Fermi level, which dominates the main features. Second, there are no other extraneous bands around the band crossings. To study the features of unconventional fermion, we construct the low-energy effective $k \cdot p$ model for the three points. We find that the threefold point has a quadratic dispersion which is dramatically different from the spin-1 fermion with linear dispersions in all directions. The Dirac point has a linear dispersion, and carries a zero topological charge since it lies in an invariant subspace of a mirror. We discovery that the sixfold degenerate point has a zero Chern number which can be regarded as a composition of two spin-1 fermions of opposite chirality, and we demonstrate it by the symmetry constrained effective Hamiltonian. Notably, we also plot the surface spectra, finding that the Fermi arcs span the whole surface Brillouin zone (BZ), which is promising to be directly observed by angle-resolved photoemission spectroscopy (ARPES). Therefore, the R_2C_3 family compounds are excellent candidates to investigate the unconventional fermions.

II. COMPUTATIONAL METHODS

We perform first-principles calculations in the framework of DFT. All calculations in our work were done using the Vienna *ab initio* simulation package (VASP) [64]. Ion cores adopt the projector augmented wave pseudopotentials [65] to model. For the exchange correlation potential, we adopt the generalized gradient approximation (GGA) of the Perdew-Burke-Ernzerhof (PBE) functional [66]. The plane wave basis energy cutoff was set as 500 eV. A Γ-centered k mesh of $11 \times 11 \times 11$ was used for BZ sampling. For the rare-earth elements, we executed GGA + U calculations to describe the Coulomb interaction [67]. The effective Coulomb energy U_{eff} was set as 3 eV, and we found the band structures will not change in a large range of U values (0–5 eV) [68]. The topological features of surface states were calculated based on the maximally localized Wannier functions [69,70], realized by using the WANNIERTOOLS package [71].

III. CRYSTAL STRUCTURE

The R_2C_3 (R = Y, La, Ce, Pr, Nd, Sm, Tb, Dy, Ho, Er, Tm, Yb, Lu) materials have been synthesized in experiments
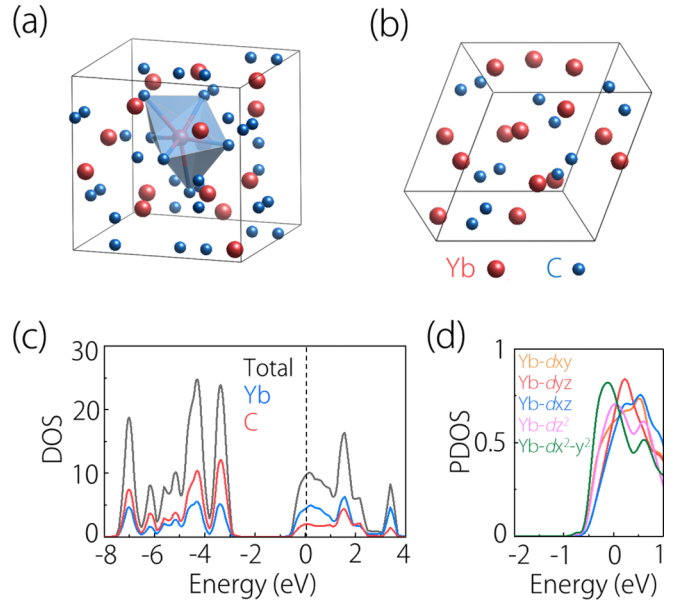

FIG. 1. (a) Unit cell and (b) primitive cell structure for Yb_2C_3. The shadowed region in (a) shows that one Yb atom is bonded to six C atoms. (c) The total density of state (DOS). (d) The projected density of state (PDOS).

[51–55]. We take Yb_2C_3 as an example to illustrate our results. Yb_2C_3 has a cubic crystal structure belonging to space group $I\bar{4}3d$ (No. 220). As shown in Fig. 1(a), one Yb atom bonds with six C atoms. In a unit cell, Yb and C atoms occupy the 16c (0.0499, 0.0499, 0.0499) and 24d (0.2937, 0, 0.25) Wyckoff sites, respectively. The fully relaxed lattice constants are $a = b = c = 8.348$Å, which match well with the experimental values ($a = b = c = 8.072$ Å [51]). Figure 1(b) shows the primitive cell of Yb_2C_3 with 8 Yb and 12 C atoms. The optimized and experimental lattices of all materials in the

TABLE I. The optimized and experimental lattice parameters and the energy positions of multifold degeneracy points (in units of eV) for R_2C_3 (R = Y, La, Ce, Pr, Nd, Sm, Tb, Dy, Ho, Er, Tm, Yb, Lu) compounds. Here OL and EL stand for optimized and experimental lattices. SP, TP, and FP stand for the sixfold, threefold, and fourfold points, respectively.

| Compound	OL (Å)	EL (Å)	Ref.	SP (eV)	TP (eV)	FP (eV)
Y_2C_3	8.264	8.234	51	−0.773	−0.998	−0.781
La_2C_3	8.819	8.817	52	−0.559	−1.013	−0.614
Ce_2C_3	8.405	8.448	52	−0.661	−1.281	−0.751
Pr_2C_3	8.700	8.590	53	−0.666	−1.021	−0.662
Nd_2C_3	8.617	8.534	53	−0.683	−1.033	−0.681
Sm_2C_3	8.477	8.399	54	−0.714	−1.043	−0.716
Tb_2C_3	8.289	8.253	52	−0.762	−1.057	−0.775
Dy_2C_3	8.237	8.206	53	−0.778	−1.062	−0.798
Ho_2C_3	8.189	8.144	55	−0.793	−1.067	−0.820
Er_2C_3	8.143	8.132	51	−0.809	−1.072	−0.843
Tm_2C_3	8.090	8.092	51	−0.828	−1.082	−0.874
Yb_2C_3	8.348	8.072	51	0.194	−0.004	−0.011
Lu_2C_3	8.011	8.035	51	−0.856	−1.079	−0.912
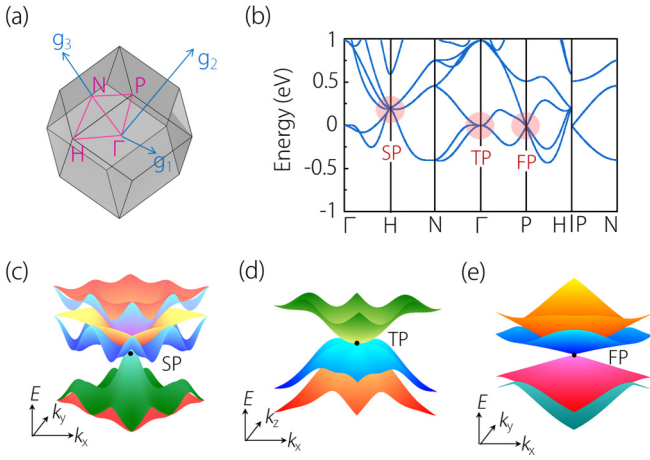
FIG. 2. (a) The bulk Brillouin zone for Yb_2C_3. (b) Electronic band structure for Yb_2C_3 without SOC. The shadowed regions show the positions of sixfold, threefold, and fourfold points, which are labeled as SP, TP, and FP, respectively. (c)–(e) Shown are the three-dimensional plots of band dispersions near SP, TP, and FP.

R_2C_3 family compounds have been summarized in Table I. In our calculations, we adopt the optimized lattice structures.

IV. TOPOLOGICAL BAND STRUCTURE

A. Symmetry analysis and $k \cdot p$ model

We plot the total density of states (DOS) and the projected density of states (PDOS) of the Yb_2C_3 compound in the absence of spin-orbit coupling (SOC) in Figs. 1(c) and 1(d). One can observe that the bands around the Fermi level are mainly contributed by the d orbitals from Yb atoms. Figure 2(b) shows the band structure of Yb_2C_3 without SOC

along high symmetry paths. One can notice that there exist three band crossings, namely, a sixfold point at the H point, a threefold point at the Γ point, and a fourfold point at the P point. Importantly, these multifold-degenerate points are very close to the Fermi level without other extraneous bands. Thus, they are promising for experimental observations in the near future. Also, the materials show no magnetic ordering, thus the time-reversal symmetry (T) is preserved. Considering the nonsymmorphic crystalline symmetries, they together protect these unconventional excitations.

Let us first study the sixfold band crossing at the H point. The sixfold degenerate point is near the Fermi level (locating at 0.194 eV). It is formed by four electronlike bands and two holelike bands, consistent with the 3D band structure that one observes in Fig. 2(c). Along the Γ-H line in Fig. 2(b), the sixfold band splits into four singly degenerate bands and one doubly degenerate band. Symmetry analysis shows that five bands belong to irreducible representations Γ_3, Γ_3, Γ_1, $\Gamma_2 + \Gamma_4$, and Γ_1 of the C_{2v} symmetry. In the other path, the H-N line, the sixfold degenerate bands split into three twofold degenerate bands protected by $\tilde{M}_{1-10}$ and T symmetries. They have same irreducible representations $\Gamma_1 + \Gamma_2$ of the C_s symmetry.

One has checked that the topological charge of this sixfold point is zero which can be demonstrated by the effective Hamiltonian. The little group of it belongs to T_d which is generated by $\{S_{4x}^{-1} \mid \frac{1}{2}00\}$, $\{\tilde{M}_{110} \mid \frac{1}{2}00\}$, and $\{C_{3,1\bar{1}\bar{1}}^{-1} \mid 1\frac{1}{2}\frac{1}{2}\}$. The irreducible representation of the sixfold band at H is the superposition of Γ_4 and Γ_5. To characterize the topology of the sixfold excitation, we have constructed an effective $k \cdot p$ model around this band crossing at H. Taking the Γ_4 and Γ_5 irreducible representations as the basis, after a unitary transformation, the effective Hamiltonian takes the form as follows:

$$\mathcal{H}(k) = \begin{bmatrix} 0 & -ivk_x & -ivk_y & 0 & -v'k_x & v''k_y \\ ivk_x & 0 & ivk_z & -v''k_x & 0 & v'k_z \\ ivk_y & -ivk_z & 0 & v'k_y & v''k_z & 0 \\ 0 & -v''k_x & v'k_y & 0 & ivk_x & ivk_y \\ -v'k_x & 0 & v''k_z & -ivk_x & 0 & -ivk_z \\ v''k_x & v'k_z & 0 & -ivk_y & ivk_z & 0 \end{bmatrix}. \tag{1}$$

We should point out that, in a limitation that $v \gg v'$ and $v \gg v''$, the Hamiltonian can be rewritten as

$$\mathcal{H}(k) = \begin{bmatrix} vk \cdot s & 0 \\ 0 & -vk \cdot s \end{bmatrix}. \tag{2}$$

Here, S is the angular momentum for the spin-1 fermion, which satisfies that $[S_i, S_j] = i\epsilon_{ijk}S_k$. Consequently, this sixfold point is a composition of two spin-1 fermions of opposite helicity. As the conventional Dirac point, it also shows a zero topological charge.

Turn to the threefold band crossing at the Γ point. Figure 2(b) shows the electronic structure for it along the N-Γ-P path without SOC. Along the N-Γ line in Fig. 2(b),

the threefold band split into three singly degenerate bands, which belong to irreducible representations Γ_2, Γ_1, and Γ_1 of the C_s symmetry. In the other path, the Γ-P line, the threefold degenerate bands split into one twofold degenerate band and one singly degenerate band. Their irreducible representations are Γ_3 (2) and Γ_1 (1) of the C_{3v} symmetry. It is worth pointing out that it shows a quadratic dispersion along Γ-N and Γ-P paths, consistent with its 3D band structure in Fig. 2(d). To characterize the nature of this quadratic threefold excitation, we also establish an effective Hamiltonian via symmetry analysis. For the Γ point, its little group T_d has four generators $\{C_{3,111}^{-} \mid 000\}$, $\{C_{2z} \mid \frac{1}{2}0\frac{1}{2}\}$, $\{C_{2x} \mid \frac{1}{2}\frac{1}{2}0\}$, and $\{\tilde{M}_{110} \mid \frac{1}{2}00\}$, and the irreducible representation at Γ is chosen as Γ_5. Together with time reversal symmetry, the effective Hamiltonian

constrained by symmetries is expressed as

$$\mathcal{H}(k)$$
$$= \begin{bmatrix} \alpha(k_x^2 + k_y^2) & i(\beta_- k_+^2 + \beta_+ k_-^2) & -\gamma k_- k_z \\ -i(\beta_+ k_+^2 + \beta_- k_-^2) & \alpha(k_x^2 + k_y^2) & i\gamma k_+ k_z \\ -\gamma_+ k_z & -i\gamma k_- k_z & 2\alpha k_z^2 \end{bmatrix},$$
(3)

with $k_\pm = k_x \pm ik_y$, and α, γ are real parameters, $\beta_\pm = (2\alpha \pm \sqrt{2}\gamma)/4$. Particularly, the position of the TP point is almost at the Fermi level, which can be read from Table I. To be noted, although the quadratic TP point has been proposed in some materials, there is no ideal candidate. Our work provides an ideal candidate to study this kind of unconventional fermion.

Lastly, we discuss the fourfold point at the P point. As shown in Fig. 2(b), the fourfold degenerate point is a result of the crossing of two nondegenerate bands and one double-degenerate band along path Γ-P-H. In detail, the double degenerate band and two singly degenerate bands separately belong to irreducible representations Γ_3 (2), Γ_1 (1), and Γ_2 (1) of the C_{3v} symmetry. Notably, the 3D band structure [see in Fig. 2(e)] for the P point indicates that it has a linear dispersion. To confirm its topology, we construct an effective model around the band crossings at P. There are four independent generators at the P point, namely, $\{C_{3,\bar{1}11}^+ \mid 0\frac{1}{2}\frac{1}{2}\}$, $\{C_{2y} \mid 0\frac{1}{2}\frac{1}{2}\}$, $\{C_{2x} \mid \frac{3}{2}\frac{3}{2}0\}$, and $\{S_{4x}^+ \mid \frac{1}{2}11\}$. The irreducible representation for the fourfold degenerate band at P is Γ_3. With the constraints from symmetries, we expand the model up to the first order which is given as

$$\mathcal{H}_{\text{Dirac}}(k)$$
$$= \begin{bmatrix} 0 & Ck_- & -Ae^{i\theta_1}k_z & Be^{-i\theta_2}k_+ \\ Ck_+ & 0 & Be^{-i\theta_2}k_- & Ae^{i\theta_1}k_z \\ -Ae^{-i\theta_1}k_z & Be^{i\theta_2}k_+ & 0 & Ck_- \\ Be^{i\theta_2}k_- & Ae^{-i\theta_1}k_z & Ck_+ & 0 \end{bmatrix}.$$
(4)

Here, A, B, C, θ_1, and θ_2 are real parameters, with $C = (\alpha + \beta)/\sqrt{6}$, and $A = |3\alpha - i(\alpha + 4\beta)|$, $B = |3\beta + i(2\alpha + \beta)|$, $\theta_1 = \arg[3\alpha - i(\alpha + 4\beta)]$, $\theta_2 = \arg[3\beta + i(2\alpha + \beta)]$. Such an effective Hamiltonian clearly exhibits a linear dispersion around the FP. Along an axis, say k_y, one can derive the four-band dispersion as

$$E_{1,2} = \sqrt{2(5\alpha^2 - 4\alpha\beta + 8\beta^2)}k_y,$$
(5)

$$E_{3,4} = -\sqrt{2(5\alpha^2 - 4\alpha\beta + 8\beta^2)}k_y.$$
(6)

Then, there exists a fourfold degenerate point at $k_y=0$. It can also be applied to the other two axes; linear dispersions also can be derived. Since P point lies on the invariant subspace of the mirror $M_{1\bar{1}0}$, the Dirac point here therefore carries a zero topological charge.

We have demonstrated that the different excitations are stabilized by the crystalline symmetries. The most fascinating discovery is that the sixfold excitation carrying a zero topological charge can be regarded as a composition of two spin-1 fermions. And the fourfold point also carries a zero Chern
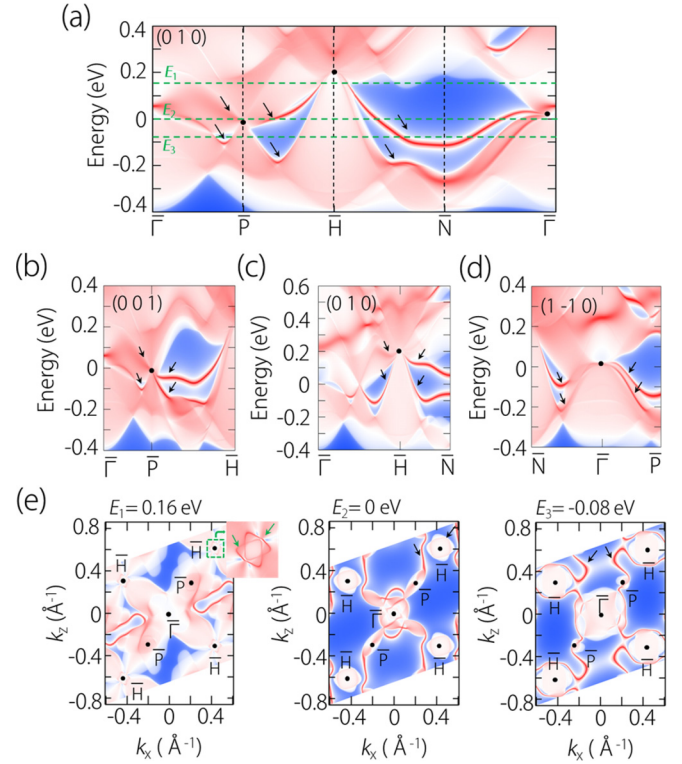

FIG. 3. (a) Projected spectrum on the (0 1 0) surface of Yb_2C_3. The black dot indicates the positions of the fourfold, sixfold, and threefold points. Two Fermi arcs (pointed by arrows) connect these multifold-degenerate points. (b)–(d) Surface states of other projective or opposite terminating surfaces with clearer Fermi arcs. (e) The corresponding constant energy slice for (a) at $E_1 = 0.16$ eV, $E_2 = 0$ eV, and $E_3 = -0.08$ eV. The arrows point to Fermi arcs.

number. Next, we focus on the topological surface Fermi arcs for them.

B. Surface states

A nontrivial topological phase implies the presence of surface states. We plot the surface spectrum for Yb_2C_3 on the plane (0 1 0) [see in Fig. 3(a)], in which two Fermi arcs are emanating from the projections (i.e., $\bar{P}$, $\bar{H}$, and $\bar{\Gamma}$) of the band crossings, including SP, FP, and TP. We also plot the enlarged images for surface spectra in Figs. 3(b)–3(d) on different surfaces; Fermi arcs also can be clearly observed. Most interestingly, we find that the surface states are extended in the whole BZ. The clear and extended Fermi arc states on different surfaces can greatly facilitate their detections in future experiments. The reason for it may be that these fermionic excitations reside in either the center or the corner of the BZ; the surface states that connect their projections emerge extensively on the side surface. In addition, we also calculated the constant energy slices near $\bar{P}$, $\bar{H}$, and $\bar{\Gamma}$ corresponding to Fig. 3(a) (at $E_1 = 0.16$ eV, $E_2 = E_F$, and $E_3 = -0.08$ eV), as shown in Fig. 3(e). Particularly, such an extended Fermi surface state can be easily identified at the Fermi energy, which provides a good candidate to experimentally study the unconventional fermions.

C. Effects of strain

Based on the slope of the crossing bands, a nodal point can be classified into type-I and type-II classes. On the other hand, they also can be classified into distinct categories according to their energy dispersions around the band crossings, namely linear, quadratic, and cubic Weyl points. For nodal lines, depending on the type of nodal points on them, it is proposed that type-I, type-II, and hybrid-type nodal lines. When all the points on the nodal line are type-I (type-II), the nodal line corresponds to type-I (type-II) [72–75]; if the nodal line possesses both type-I and type-II nodal points, it belongs to the hybrid type [76,77]. Many interesting properties have been proposed for each type of nodal points and nodal lines. In our work, we can realize these distinct topological phases by symmetry breaking via strain. Here, we take Yb_2C_3 as an example.

First, we use a compressive strain along [001] to break the threefold rotation along [111] direction. One can see that it makes the sixfold point split into three twofold degenerate points at the H point due to the breaking of $C_{3,111}$. These three points are not isolated, but points belonging to nodal lines on path H-N. Meanwhile, there emerges a type-II Weyl point on path Γ-H. Turning to the threefold point at Γ point, there is a single band keeping away from the degenerate point, and a type-I quadratic Weyl point appears at the Γ point which almost lies at the Fermi level [see Fig. 4(e)]. A type-II Weyl point also emerges on the Γ-N path. In Fig. 4(h), under a [0 0 1] direction strain, the fourfold point is separated into two double degenerate points at the P point.

Second, we consider a strain along the [1 1 1] direction. Then, the sixfold point at the H point is transformed into a fourfold point and a twofold degenerate point, and the twofold point is also a point on the nodal line along path H-N [see in Fig. 4(c)]. Such a strain makes the threefold point at the Γ point split into one twofold degenerate point and one singly degenerate band [see Fig. 4(f)]. Besides, there are also emerging a type-I Weyl point along the N-Γ path and a threefold point along the Γ-P line. The fourfold point is transformed into one double degenerate point which is a point on the nodal line on path P-Γ and two singly degenerate bands [see Fig. 4(i)]. Moreover, there emerge threefold points on path Γ-P, together with a nodal line along Γ-P and a nodal loop around the P point. Notably, for each k path (P-a, P-b, P-c, and P-d) from the P point in the plane, we can obtain both type-I and type-II band crossings, as shown in Fig. 4(j). It is evident that the nodal loop in Fig. 4(i) is a hybrid nodal loop. Here, we should address the difference between threefold points along Γ-P and the one appearing at the Γ point model: First, the former one appearing on the high symmetry path is the crossing between 2D and a 1D irreducible representations. However, the latter occurs at a high symmetry point which is in a 3D irreducible representation. Second, the former one is accompanied by nodal lines; the topology is strongly related to the Berry phase of nodal lines [78]. The topology of the latter one is exhibited by its topological charge and corresponding surface states.

Beyond the strain, when SOC is taken into consideration, the topological phases would experience a transformation.
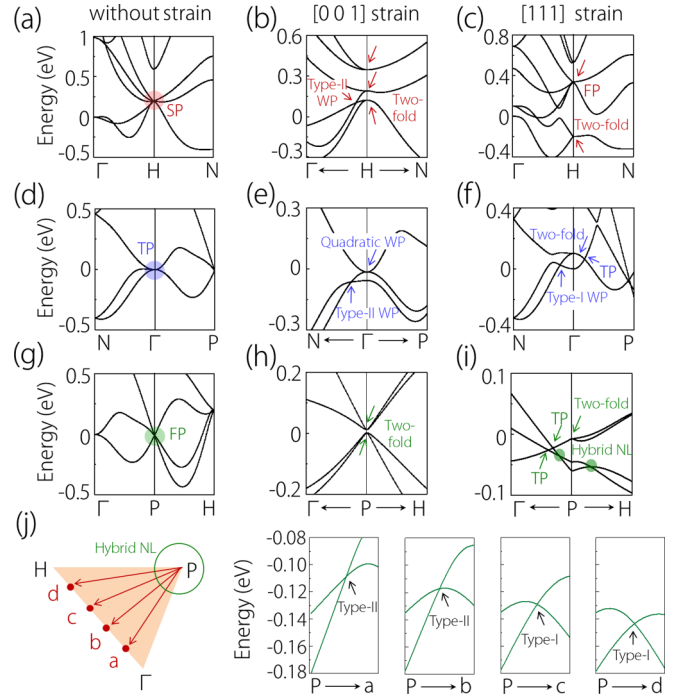

FIG. 4. Bulk band structures along the Γ-H-N path without strain (a), with [0 0 1] strain (b), and with [1 1 1] strain (c). Bulk band structures along the N-Γ-P path without strain (d), with [0 0 1] strain (e), and with [1 1 1] strain (f). Bulk band structures along the Γ-P-H path without strain (g), with [0 0 1] strain (h), and with [1 1 1] strain (i). (j) Schematic illustration of the hybrid-type nodal line in (i) centering on the P point in the H-P-Γ plane. Crossing the nodal line, we choose four k paths, namely P-a, P-b, P-c, and P-d. The points a, b, c, and d are equally spaced between Γ and H. Electronic band structures of Yb_2C_3 at the P-a, P-b, P-c, and P-d paths display the nodal line that possesses both type-I and type-II band crossings. SP, sixfold point; FP, fourfold point; TP, threefold point; WP, Weyl point; NL, nodal line.

We discuss the case with SOC in the Supplemental Material. We also find the presence of some unconventional fermions with SOC.

D. Comparison in R_2C_3 family

Figure 5 shows the electronic band structure for the R_2C_3 (R = Y, La, Ce, Pr, Nd, Sm, Tb, Dy, Ho, Er, Tm, Yb, Lu) family of materials in the absence of SOC. One can observe that they share a similar band structure; three unconventional fermions can be discovered in corresponding high symmetry points. Generally, there is a trend (from Y to Lu) that the degenerate point should appear in a much lower energy as the increment of valance electrons (see in Table I). However, one can easily observe that the material Yb_2C_3 is the best candidate. This result may be attributed to the electron filling. Among these rare-earth elements, only the Yb atom has full filled orbitals, leading to a weaker orbital hybridization. We take the neighbors of Yb as comparisons, considering R=Tm, Yb, Lu. We plot the DOS [68]; the bands around the Fermi level are mainly contributed by the p, d orbits. Here, d orbits
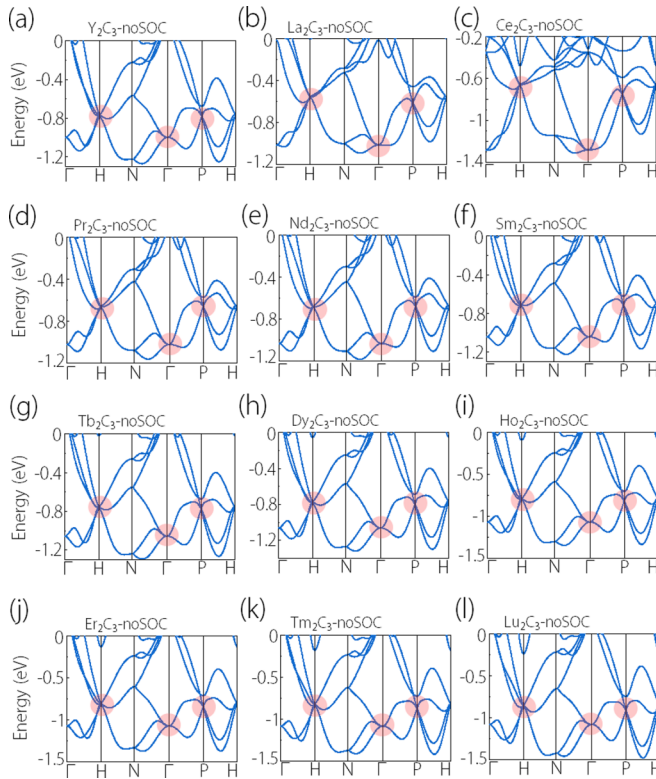
FIG. 5. Electronic band structures of (a) Y_2C_3, (b) La_2C_3, (c) Ce_2C_3, (d) Pr_2C_3, (e) Nd_2C_3, (f) Sm_2C_3, (g) Tb_2C_3, (h) Dy_2C_3, (i) Ho_2C_3, (j) Er_2C_3, (k) Tm_2C_3, and (l) Lu_2C_3 without SOC. The multifold degeneracy points are highlighted by red shadowed regions. Sixfold point is at the H point; threefold point is at the Γ point; fourfold point is at the P point.

are from rare earth and p are from C and rare-earth elements except Lu. Comparing the DOSs, one can easily observe that the hybridizations in Tm_2C_3 and Lu_2C_3 are indeed stronger than those in Yb_2C_3. More states appear in bonding orbitals Tm_2C_3 and Lu_2C_3, leading to the band crossings dropping down below the Fermi level. In sharp contrast, states prefer to occur in low energy in Yb_2C_3, and the degenerate points are therefore lifted. Consequently, the realistic material Yb_2C_3 is the best candidate. We should emphasize that this family of materials shares a similar electronic band structure; although degenerate points in materials ($R = $ Y, La, Ce, Pr, Nd, Sm, Tb, Dy, Ho, Er, Tm, Lu) locate far from the Fermi level, there are no other extraneous bands around them at their energy level.

V. DISCUSSION AND CONCLUSION

Before closing, we have several remarks. First, the most important finding here is that we propose a family of materials, R_2C_3, which realizes multiple types of unconventional fermions, including the six-, four- and threefold fermions. We emphasize that the realistic material Yb_2C_3 is an ideal candidate to study these unconventional fermions. It has advantages over others. (i) The band crossings in the Yb_2C_3 electronic band structure are closed to the Fermi level. Particularly, the TP points almost lie at the Fermi level. (ii) It has a "clean" band structure without other rambling bands nearby. (iii) Yb_2C_3 has clear "Fermi arcs" corresponding to unconventional fermions. As shown in Fig. 3, the surface states emerge from the projections of unconventional fermions, and extensively exist on the side surfaces. Moreover, these surface states are within a wide energy window. Thus, it is easy to detect the unconventional fermions in experiments.

Second, taking Yb_2C_3 as an example, we can realize a phase transition by using strain, leading to various topological phases. (i) Under a [0 0 1] direction strain, these points can be transformed to type-I quadratic and type-II linear Weyl points. (ii) With a strain in the [1 1 1] direction, one can derive more fruit phases, including fourfold, threefold, type-I Weyl points, and a hybrid-type nodal line. When SOC is considered, there still exist unconventional fermions in these materials. As shown in Fig. S3 [68], there exist fourfold and eightfold (higher degeneracy) band crossings. It indicates that the study still is meaningful after considered SOC.

In conclusion, by using first-principles calculations, we predict that bulk R_2C_3 family compounds host sixfold, threefold, and fourfold fermions in the absence of SOC. Even when the U value varies from 0 eV to 5 eV (see Supplemental Material), the multifold degeneracy points are still stable. Most importantly, Yb_2C_3 is an ideal material for studying unconventional quasiparticles in conventional crystals for its advantages over other materials. Thereby, R_2C_3 family compounds, especially Yb_2C_3, can serve as new platforms for the study of unconventional quasiparticles in near future experiments.

[1] P. B. Pal, Am. J. Phys. **79**, 485 (2011).

[2] L. R. Wang, L. Jin, G. D. Liu, Y. Liu, X. F. Dai, and X. M. Zhang, Appl. Mater. Today. **23**, 101057 (2021).

[3] X. T. Wang, Z. X. Cheng, G. Zhang, H. K. Yuan, H. Chen, and X.-L. Wang, Phys. Rep. **888**, 1 (2020).

[4] Y. Wang, L. Wang, J. Xia, Z. Lai, G. Tian, X. Zhang, Z. Hou, X. Gao, W. Mi, C. Feng, M. Zeng, G. Zhou, G. Yu, G. Wu, Y. Zhou, W. Wang, X.-X. Zhang, and J. Liu, Nat. Commun. **11**, 3577 (2020).

[5] Y. Liu, Z.-M. Yu, C. Xiao, and S. A. Yang, Phys. Rev. Lett. **125**, 076801 (2020).

[6] X. Wan, A. M. Turner, A. Vishwanath, and S. Y. Savrasov, Phys. Rev. B **83**, 205101 (2011).

[7] H. Weng, C. Fang, Z. Fang, B. A. Bernevig, and X. Dai, Phys. Rev. X **5**, 011029 (2015).

[8] B. Q. Lv, H. M. Weng, B. B. Fu, X. P. Wang, H. Miao, J. Ma, P. Richard, X. C. Huang, L. X. Zhao, G. F. Chen, Z. Fang, X. Dai, T. Qian, and H. Ding, Phys. Rev. X **5**, 031013 (2015).

[9] Y. Xu, F. Zhang, and C. Zhang, Phys. Rev. Lett. **115**, 265304 (2015).

[10] Z. Wang, D. Gresch, A. A. Soluyanov, W. Xie, S. Kushwaha, X. Dai, M. Troyer, R. J. Cava, and B. A. Bernevig, Phys. Rev. Lett. **117**, 056805 (2016).

[11] G. Autès, D. Gresch, M. Troyer, A. A. Soluyanov, and O. V. Yazyev, Phys. Rev. Lett. **117**, 066402 (2016).

[12] G. Chang *et al.*, Sci. Adv. **2**, e1600295 (2016).

[13] J. Ruan, S. K. Jian, H. Yao, H. Zhang, S. C. Zhang, and D. Xing, Nat. Commun. **7**, 11136 (2016).

[14] J. Ruan, S. K. Jian, D. Zhang, H. Yao, H. Zhang, S.-C. Zhang, and D. Xing, Phys. Rev. Lett. **116**, 226801 (2016).

[15] W. Z. Meng, X. M. Zhang, T. L. He, L. Jin, X. F. Dai, Y. Liu, and G. D. Liu, J. Adv. Res. **24**, 523 (2020).

[16] G. Sharma, P. Goswami, and S. Tewari, Phys. Rev. B **96**, 045112 (2017).

[17] S. M. Young, S. Zaheer, J. C. Y. Teo, C. L. Kane, E. J. Mele, and A. M. Rappe, Phys. Rev. Lett. **108**, 140405 (2012).

[18] Z. Wang, H. Weng, Q. Wu, X. Dai, and Z. Fang, Phys. Rev. B **88**, 125427 (2013).

[19] Y. X. Zhao and Z. D. Wang, Phys. Rev. Lett. **110**, 240404 (2013).

[20] Z. K. Liu, B. Zhou, Y. Zhang, Z. J. Wang, H. M. Weng, D. Prabhakaran, S.-K. Mo, Z. X. Shen, Z. Fang, X. Dai, Z. Hussain, and Y. L. Chen, Science **343**, 864 (2014).

[21] M. Neupane, S.-Y. Xu, R. Sankar, N. Alidoust, G. Bian, C. Liu, I. Belopolski, T.-R. Chang, H.-T. Jeng, H. Lin, A. Bansil, F. C. Chou, and M. Z. Hasan, Nat. Commun. **5**, 3786 (2014).

[22] Z. K. Liu, J. Jiang, B. Zhou, Z. J. Wang, Y. Zhang, H. M. Weng, D. Prabhakaran, S.-K. Mo, H. Peng, P. Dudin, T. Kim, M. Hoesch, Z. Fang, X. Dai, Z. X. Shen, D. L. Feng, Z. Hussain, and Y. L. Chen, Nat. Mater. **13**, 677 (2014).

[23] S.-Y. Xu, C. Liu, S. K. Kushwaha, R. Sankar, J. W. Krizan, I. Belopolski, M. Neupane, G. Bian, N. Alidoust, T.-R. Chang, H.-T. Jeng, C.-Y. Huang, W.-F. Tsai, H. Lin, P. P. Shibayev, F.-C. Chou, R. J. Cava, and M. Z. Hasan, Science **347**, 294 (2015).

[24] Y. Du, F. Tang, D. Wang, L. Sheng, E.-J. Kan, C.-G. Duan, S. Y. Savrasov, and X. Wan, npj Quantum Mater. **2**, 3 (2017).

[25] T. L. He, Y. Liu, L. Tian, X. M. Zhang, W. Z. Meng, X. F. Dai, and G. D. Liu, Phys. Rev. B **103**, 085135 (2021).

[26] L. Jin, L. R. Wang, X. M. Zhang, Y. Liu, X. F. Dai, H. L. Gao, and G. D. Liu, Nanoscale **13**, 5901 (2021).

[27] F. Tang, H. C. Po, A. Vishwanath, and X. Wan, Nature (London) **566**, 486 (2019).

[28] T. Zhang, Y. Jiang, Z. Song, H. Huang, Y. He, Z. Fang, H. Weng, and C. Fang, Nature (London) **566**, 475 (2019).

[29] B. Bradlyn, J. Cano, Z. Wang, M. Vergniory, C. Felser, R. Cava, and B. A. Bernevig, Science **353**, aaf5037 (2016).

[30] B. J. Wieder, Y. Kim, A. M. Rappe, and C. L. Kane, Phys. Rev. Lett. **116**, 186402 (2016).

[31] H. Weng, C. Fang, Z. Fang, and X. Dai, Phys. Rev. B **94**, 165201 (2016).

[32] H. Weng, C. Fang, Z. Fang, and X. Dai, Phys. Rev. B **93**, 241202(R) (2016).

[33] Z. Zhu, G. W. Winkler, Q. S. Wu, J. Li, and A. A. Soluyanov, Phys. Rev. X **6**, 031003 (2016).

[34] B. Lv *et al.*, Nature (London) **546**, 627 (2017).

[35] L. Jin, X. M. Zhang, Y. Liu, X. F. Dai, L. Y. Wang, and G. D. Liu, Phys. Rev. B **102**, 195104 (2020).

[36] P. Tang, Q. Zhou, and S.-C. Zhang, Phys. Rev. Lett. **119**, 206402 (2017).

[37] D. Takane, Z. Wang, S. Souma, K. Nakayama, T. Nakamura, H. Oinuma, Y. Nakata, H. Iwasawa, C. Cacho, T. Kim, K. Horiba, H. Kumigashira, T. Takahashi, Y. Ando, and T. Sato, Phys. Rev. Lett. **122**, 076402 (2019).

[38] T. Zhang, Z. Song, A. Alexandradinata, H. Weng, C. Fang, L. Lu, and Z. Fang, Phys. Rev. Lett. **120**, 016401 (2018).

[39] Z. Rao, H. Li, T. Zhang, S. Tian, C. Li, B. Fu, C. Tang, L. Wang, Z. Li, W. Fan, J. Li, Y. Huang, Z. Liu, Y. Long, C. Fang, H. Weng, Y. Shi, H. Lei, Y. Sun, T. Qian, and H. Ding, Nature (London) **567**, 496 (2019).

[40] G. Chang, S.-Y. Xu, B. J. Wieder, D. S. Sanchez, S.-M. Huang, I. Belopolski, T.-R. Chang, S. Zhang, A. Bansil, H. Lin, and M. Z. Hasan, Phys. Rev. Lett. **119**, 206401 (2017).

[41] Q.-Q. Yuan, L. Zhou, Z.-C. Rao, S. Tian, W.-M. Zhao, C.-L. Xue, Y. Liu, T. Zhang, C.-Y. Tang, Z.-Q. Shi, Z.-Y. Jia, H. Weng, H. Ding, Y.-J. Sun, H. Lei, and S.-C. Li, Sci. Adv. **5**, eaaw9485 (2019).

[42] F. Flicker, F. de Juan, B. Bradlyn, T. Morimoto, M. G. Vergniory, and A. G. Grushin, Phys. Rev. B **98**, 155145 (2018).

[43] F. de Juan, A. G. Grushin, T. Morimoto, and J. E. Moore, Nat. Commun. **8**, 15995 (2017).

[44] N. B. M. Schröter, D. Pei, M. G. Vergniory, Y. Sun, K. Manna, F. D. Juan, J. A. Krieger, V. Süss, M. Schmidt, P. Dudin, B. Bradlyn, T. K. Kim, T. Schmitt, C. Cacho, C. Felser, V. N. Strocov, and Y. Chen, Nat. Phys. **15**, 759 (2019).

[45] Z. P. Sun, C. Q. Hua, X. L. Liu, Z. T. Liu, M. Ye, S. Qiao, Z. H. Liu, J. S. Liu, Y. F. Guo, Y. H. Lu, and D. W. Shen, Phys. Rev. B **101**, 155114 (2020).

[46] X. Yáng, T. A. Cochran, R. Chapai, D. Tristant, J.-X. Yin, I. Belopolski, Z. Chéng, D. Multer, S. S. Zhang, N. Shumiya, M. Litskevich, Y. Jiang, G. Chang, Q. Zhang, I. Vekhter, W. A. Shelton, R. Jin, S.-Y. Xu, and M. Z. Hasan, Phys. Rev. B **101**, 201105(R) (2020).

[47] N. Kumar, M. Yao, J. Nayak, M. G. Vergniory, J. Bannies, Z. Wang, N. B. M. Schröter, V. N. Strocov, L. Müchler, W. Shi, E. D. L. Rienks, J. L. Mañes, C. Shekhar, S. S. P. Parkin, J. Fink, G. H. Fecher, Y. Sun, B. A. Bernevig, and C. Felser, Adv. Mater. **32**, 1906046 (2020).

[48] S. Thirupathaiah, Y. S. Kushnirenko, K. Koepernik, B. R. Piening, B. Büchner, S. Aswartham, J. V. D. Brink, S. V. Borisenko, and I. C. Fulga, SciPost Phys. **10**, 004 (2021).

[49] S. Nie, B. A. Bernevig, and Z. Wang, Phys. Rev. Research **3**, 012028 (2021).

[50] X. Zhang, Q. Gu, H. Sun, T. Luo, Y. Liu, Y. Chen, Z. Shao, Z. Zhang, S. Li, Y. Sun, Y. Li, X. Li, S. Xue, J. Ge, Y. Xing, R. Comin, Z. Zhu, P. Gao, B. Yan, J. Feng, M. Pan, and J. Wang, Phys. Rev. B **102**, 035125 (2020).

[51] V. I. Novokshonov, Zh. Neorg. Khim. **25**, 684 (1980) [Russ. J. Inorg. Chem. **25**, 375 (1980)].

[52] M. Atoji and D. E. Williams, J. Chem. Phys. **35**, 1960 (1961).

[53] M. Atoji, J. Solid. State. Chem. **26**, 51 (1978).

[54] F. H. Spedding, K. A. J. Gschneidner, and A. H. Daane, J. Am. Chem. Soc. **80**, 4499 (1958).

[55] M. Atoji and Y. Tsunoda, J. Chem. Phys. **54**, 3510 (1971).

[56] K. Sugawara, T. Sato, S. Souma, T. Takahashi, and A. Ochiai, Phys. Rev. B **76**, 132512 (2007).

[57] J. S. Kim, R. K. Kremer, O. Jepsen, and A. Simon, Curr. Appl. Phys. **6**, 897 (2006).

[58] S. Akutagawa and J. Akimitsu, Sci. Technol. Adv. Mat. **7**, 2 (2006).

[59] G. Amano, S. Akutagawa, T. Muranaka, Y. Zenitani, and J. Akimitsu, J. Phys. Soc. Jpn. **73**, 530 (2004).

[60] D. J. Singh and I. I. Mazin, Phys. Rev. B **70**, 052504 (2004).

[61] Y. Nishikayama, T. Shishidou, and T. Oguchi, J. Phys. Soc. Jpn. **76**, 064714 (2007).

[62] A. I. Kriklya, A. S. Bolgar, and A. P. Suodis, Powder Metall. Met. Ceram **36**, 405 (1997).

[63] J. S. Kim, W. Xie, R. K. Kremer, V. Babizhetskyy, O. Jepsen, A. Simon, K. S. Ahn, B. Raquet, H. Rakoto, J. M. Broto, and B. Ouladdiaf, Phys. Rev. B **76**, 014516 (2007).

[64] G. Kresse and D. Joubert, Phys. Rev. B **59**, 1758 (1999).

[65] P. E. Blöchl, Phys. Rev. B **50**, 17953 (1994).

[66] J. P. Perdew, K. Burke, and M. Ernzerhof, Phys. Rev. Lett. **77**, 3865 (1996).

[67] V. I. Anisimov, J. Zaanen, and O. K. Andersen, Phys. Rev. B **44**, 943 (1991).

[68] See Supplemental Material at http://link.aps.org/supplemental/10.1103/PhysRevB.104.045111 for the considered band structures of Yb_2C_3 under different U values, DOS, and PDOS of Tm_2C_3, Yb_2C_3, Lu_2C_3, and band structures of Yb_2C_3 with SOC.

[69] N. Marzari and D. Vanderbilt, Phys. Rev. B: Condens. Matter Mater. Phys. **56**, 12847 (1997).

[70] A. A. Mostofi, J. R. Yates, Y.-S. Lee, I. Souza, D. Vanderbilt, and N. Marzari, Comput. Phys. Commun. **178**, 685 (2008).

[71] Q. S. Wu, S. N. Zhang, H.-F. Song, M. Troyer, and A. A. Soluyanov, Comput. Phys. Commun. **224**, 405 (2018).

[72] S. Li, Z.-M. Yu, Y. Liu, S. Guan, S.-S. Wang, X. M. Zhang, Y. G. Yao, and S. A. Yang, Phys. Rev. B **96**, 081106(R) (2017).

[73] X. M. Zhang, L. Jin, X. F. Dai, and G. D. Liu, J. Phys. Chem. Lett. **8**, 4814 (2017).

[74] T. L. He, X. M. Zhang, L. R. Wang, Y. Liu, X. F. Dai, L. Y. Wang, and G. D. Liu, Mater. Today Phys. **17**, 100360 (2021).

[75] L. Jin, X. M. Zhang, Y. Liu, X. F. Dai, X. N. Shen, L. Y. Wang, and G. D. Liu, Phys. Rev. B **102**, 125118 (2020).

[76] X. M. Zhang, Z.-M. Yu, Y. Lu, X.-L. Sheng, H. Y. Yang, and S. A. Yang, Phys. Rev. B **97**, 125143 (2018).

[77] T. He, X. Zhang, Y. Liu, X. Dai, G. Liu, Z. M. Yu, and Y. Yao, Phys. Rev. B **102**, 075133 (2020).

[78] G. W. Winkler, S. Singh, and A. A. Soluyanov, Chin. Phys. B **28**, 077303 (2019).